Improved two-frequency temporal phase unwrapping method in fringe projection profilometry

JINTAO LIU
Qingdao University of Technology
XU PENG
Qingdao University of Technology
SHAN SHUO
Qingdao University of Technology
ZHANG WEN
Qingdao University of Technology
ZE LI
Qingdao University of Technology
WANG JIANHUA
wjh051130@163.com
Qingdao University of Technology

Research Article

Keywords: Fringe projection profilometry, 3D measurement, Phase error

Posted Date: October 18th, 2023

DOI: https://doi.org/10.21203/rs.3.rs-3448931/v1

Additional Declarations: No competing interests reported.

Version of Record: A version of this preprint was published at Applied Physics B on February 23rd, 2024.
See the published version at https://doi.org/10.1007/s00340-024-08183-3.

Improved two-frequency temporal phase unwrapping method in fringe projection profilometry

LIU JINTAO, XU PENG, SHAN SHUO, ZHANG WEN, LI ZE AND WANG JIANHUA*

School of Information and Control Engineering, Qingdao University of Technology, Qingdao, 266520, China

**Corresponding author: wjh051130@163.com*

Abstract: In three-dimensional (3D) measurement using fringe projection profilometry (FPP), noise introduced by the camera during fringe capture can cause phase errors in the reconstructed results, affecting the accuracy of the 3D measurements. The two-frequency temporal phase unwrapping method is widely used due to its high efficiency. However, the use of only two fringe patterns in this method leads to reduced noise immunity and an increased phase error. Many researchers have focused on improving the two-frequency method, but little attention has been paid to enhancing its noise immunity. In this article, we propose a novel two-frequency phase unwrapping method. Firstly, we analyze the phase errors of the traditional $4f_h$+$4f_l$ two-frequency method and our proposed method in detail. Then, the feasibility of our proposed method is demonstrated through multiple sets of experimental results. Finally, we provide solutions to the problems encountered in our proposed method. Through experiments, our proposed method reduces the phase error by 75.90% and 91.39% relative to the traditional $4f_h$+$4f_l$ method, in metal object and gypsum board experiments, respectively. The experimental results show that our proposed method significantly improves the reliability of phase unwrapping and reduces phase errors, thus enhancing the accuracy of 3D reconstruction.

Keywords: Fringe projection profilometry; 3D measurement; Phase error

1. Introduction

Structured light three-dimensional (3D) shape measurement technique[1-6] is the kind of non-contact measurement technique, that has the advantages of high measurement accuracy, fast speed, low cost, and full field measurement. It has been widely used in heritage conservation, human modeling, industrial manufacturing, bionic design, and many other fields [7-12]. Fringe projection profilometry (FPP)[13-15] is the most representative technique in structured light 3D shape measurement [16]. Its main principle is that the projector projects grating fringes to the measured object, and the camera collects the deformed fringes caused by the modulation of the object's surface. Then, the 3D shape of the measured object can be determined by the position relationship between the camera and the projector and the extent of fringe deformation[17-22].

In fringe projection techniques, the camera captures the fringe patterns, and environmental light interference can introduce higher harmonic components into the patterns, leading to phase extraction errors. Many researchers have studied the phase errors caused by noise in phase-shifting methods. Rathjen et al. [23] established a phase error model under Gaussian noise interference and concluded that the phase error is inversely proportional to the signal-to-noise ratio. Zuo et al. [24] reduced phase error by increasing the modulation intensity of the fringe patterns in the phase-shifting method. Their method is based on the characteristic of the phase-shifting method, where the phase error is inversely proportional to the modulation intensity of the captured fringe patterns. Li et al. [25] and Servin et al. [26] demonstrated that the phase error in the phase-shifting method is inversely proportional to the modulation intensity of the captured fringe patterns, inversely proportional to the number of phase shifts, and directly

proportional to the square of the variance of random noise. Zhang et al. [27] further confirmed that the phase error in the phase-shifting method is also related to the frequency of the fringe patterns and provided a method for selecting the optimal frequency. Wang et al. [28] analyzed several non-standard phase-shifting methods based on a small number of fringe patterns and evaluated their reliability in temporal phase unwrapping using variance quantification, comparing the advantages and disadvantages of these methods for 3D measurement. Liu et al. [29] proposed a method to evaluate the noise resistance of the two-frequency phase-shifting method. They established a wrapped phase error model considering fringe noise interference and used differential calculus to obtain the maximum variance of the wrapped phase error. They then quantified and compared the variances to assess the performance of different two-frequency phase-shifting methods.

In fringe projection profilometry, many researchers have analyzed various factors that affect phase errors and proposed methods to reduce these errors by controlling those factors. However, there has not been an effective solution specifically aimed at reducing phase errors in dual-frequency phase-shifting methods. To address this issue, this paper proposes a dual-frequency heterodyne phase unwrapping method. By increasing the number of phase unwrapping steps while keeping the fringe frequency ratio unchanged, the proposed method aims to reduce phase errors in the 3D reconstruction results without introducing additional fringes. This paper begins by analyzing and comparing the principles of the traditional $4f_h+4f_l$ method and the proposed method, as well as the variances of their phase errors. Then, through three sets of comparative experiments, the correctness of the proposed method's principles is validated. Finally, it is concluded that the proposed method significantly improves the reliability of phase unwrapping, reduces phase errors, and enhances the accuracy of 3D reconstruction results.

The structure of this paper is as follows: the second chapter introduces the basic principles of FPP, the $4f_h+4f_l$ method, and the proposed method, and then analyzes the phase error of the two methods. the third chapter is the experiment and analysis, and the fourth chapter is the summary of this paper.

2. Principle

2.1 Fringe projection and capture in FPP

For FPP, the process starts by generating computer-generated sinusoidal grating fringe patterns. These patterns are then projected onto the surface of the object under measurement using a projector. Simultaneously, a camera captures both the reference fringe pattern and the deformed fringe pattern caused by the surface of the object. The captured fringe patterns are then transferred to a computer, where the wrapped phase of the captured fringes is computed. The wrapped phase contains information about the depth of the object's surface. However, since the inverse tangent function used to compute the wrapped phase results in a range of $(-\pi, \pi]$, phase unwrapping is required to obtain a continuous phase distribution. temporal phase unwrapping methods are often employed as they offer good reconstruction results for objects with high discontinuities. Finally, by performing camera calibration and phase-to-height mapping, the three-dimensional geometry of the object's surface is obtained.

The projected fringe pattern can be represented as follows：

$$I^p(x, y) = A(x, y) + B(x, y)\cos(2\pi fx), \tag{1}$$

where I^p represents the projected fringe pattern, $A(x, y)$ represents the average intensity, $B(x, y)$ represents the modulation intensity, and f is the fringe frequency.

When capturing the fringe pattern with a camera, it is affected by the reflectivity of the object's surface, ambient light, and the sensitivity of the camera. Therefore, in phase-shifting profilometry, the captured fringe pattern can be represented by Eq. (2):

$$I_n^c(x, y) = a(x,, y) + b(x, y)\cos\left[\varphi(x, y) + 2\pi n / N\right], \tag{2}$$

In which

$$\begin{cases} a(x,y) = s\kappa(x,y)[A(x,y) + r_1(x,y)] + sr_2(x,y) \\ b(x,y) = s\kappa(x,y)B(x,y) \end{cases}, \tag{3}$$

where $I_n^c(x,y)$ represents the n-th captured fringe pattern by the camera, $\varphi(x, y)$ represents the wrapped phase, s represents the sensitivity of the camera, $\kappa(x, y)$ represents the reflectivity of the object's surface, r_1 represents the ambient light reflected by the object's surface, and r_2 represents the ambient light directly entering the camera. Please refer to Fig. 1. for a visual representation.

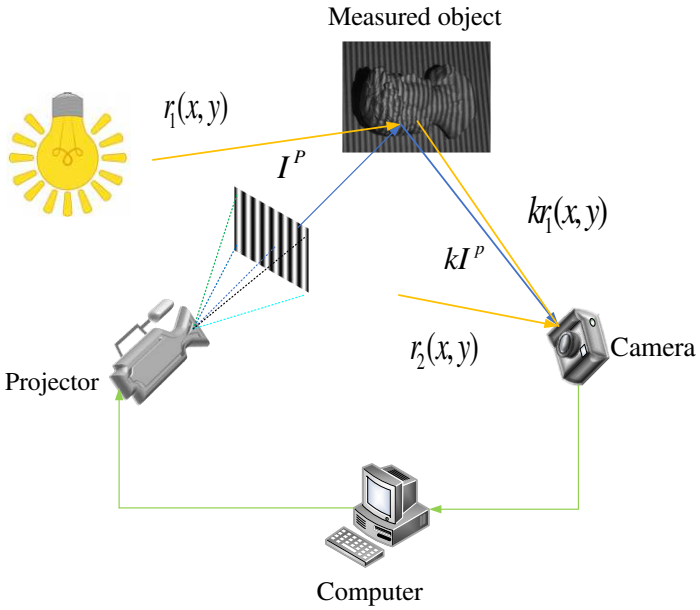

Fig. 1. Lighting model of FPP.

2.2 Wrapped phase error analysis

After capturing the fringe patterns with the camera, it is necessary to compute the wrapped phase φ(x,y) from the captured images. The wrapped phase can be represented by Eq. (4):

$$\varphi(x,y) = -\arctan\frac{\sum_{n=1}^{N} I_n(x,y)\sin[2\pi(n-1)/N]}{\sum_{n=1}^{N} I_n(x,y)\cos[2\pi(n-1)/N]}, \tag{4}$$

where n represents the n-th phase shift and N represents the total number of phase shifts.

When capturing projected fringes using a camera, it is common to introduce additive Gaussian noise. In this case, the noise has a mean of 0 and a variance of σ^2. Based on the noise model proposed by Li et al. [25], Zuo et al. [30] obtained the variance of the enveloping phase error by assuming the Gaussian distribution additive noise with a variance of σ^2, which can be expressed by Eq. (5):

$$\sigma_{\Delta\varphi}^2 = \frac{2\sigma^2}{Nb^2}. \tag{5}$$

Therefore, for the dual-frequency phase unwrapping method, according to Eq. (5), we can obtain the variance of phase wrapping errors for two frequency fringes:

$$\sigma_{\Delta\varphi-fh}^2 = \sigma_{\Delta\varphi-fl}^2 = \frac{2\sigma^2}{4b^2}. \tag{6}$$

Assuming that f_h-f_l =1, we can calculate the phase wrapping error for the frequency of 1 as:

$$\varphi_{f1} = \varphi_{fh} - \varphi_{fl} \Rightarrow \Delta\varphi_{f1} = \Delta\left(\varphi_{fh} - \varphi_{fl}\right), \tag{7}$$

$$\begin{aligned}\Delta\varphi_{f1} &= \Delta(\varphi_{fh}-\varphi_{fl}) \\ &= \left(Q_{fh}-Q_{fl}\right)-\left(\varphi_{fh}-\varphi_{fl}\right) \\ &= \left(Q_{fh}-\varphi_{fh}\right)-\left(Q_{fl}-\varphi_{fl}\right) \\ &= \Delta\varphi_{fh}-\Delta\varphi_{fl}\end{aligned}, \tag{8}$$

where Q represents the wrapping phase that introduces noise, the variance of the phase wrapping error for the frequency of 1:

$$\begin{aligned}&\sigma^2_{\Delta\varphi-f1}=\sigma^2_{(\Delta\varphi-fh)-(\Delta\varphi-fl)}=\sigma^2_{\Delta\varphi-fh}+\sigma^2_{\Delta\varphi-fl}-2Cov\left(\Delta\varphi_{fh},\Delta\varphi_{fl}\right) \\ &\Rightarrow \sigma^2_{\Delta\varphi-f1}=\sigma^2_{\Delta\varphi-fh}+\sigma^2_{\Delta\varphi-fl}=\frac{2\sigma^2}{4b^2}+\frac{2\sigma^2}{4b^2}=\frac{\sigma^2}{b^2},\end{aligned} \tag{9}$$

where $Cov(x,y)$ indicates the correlation between x and y. For the proposed method, the camera captures two sets of fringes with frequencies f_4=31 and f_3=15. It requires two heterodyne operations to obtain the wrapped phase with a frequency of 1. Therefore, the variance of the wrapped phase error with a frequency of 1 can be calculated as follows:

$$\sigma^2_{\Delta\varphi-f1}=\sigma^2_{\Delta\varphi-f3}+\sigma^2_{\Delta\varphi-f2}=\frac{2\sigma^2}{4b^2}+\frac{\sigma^2}{b^2}=\frac{3\sigma^2}{2b^2}, \tag{10}$$

where, f_2=16, f_1=1.

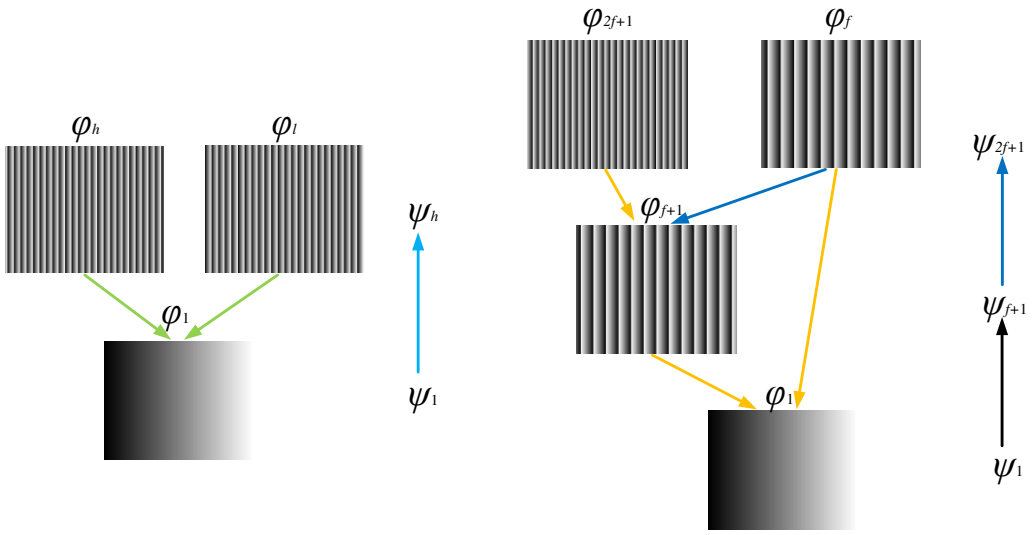

Fig. 2. Method schematic diagram.

2.3 Unwrapping phase error analysis

The phase values obtained from Eq.(4) are wrapped within the range of (-π, π], which means they do not provide a continuous phase distribution. Therefore, it is necessary to unwrap the wrapped phase, and the unwrapping of the wrapped phase can be expressed by Eq.(11).

$$\begin{cases}\psi(x,y)=\varphi(x,y)+2\pi k(x,y) \\ k(x,y)=Round\left[\dfrac{(f_h/f_l)\psi_l(x,y)-\varphi_h(x,y)}{2\pi}\right]\end{cases}, \tag{11}$$

where $\psi(x, y)$ represents the unwrapped phase, while $\varphi(x, y)$ denotes the wrapped phase. The fringe order is represented by $k(x, y)$, and it needs to be rounded to an integer using the *Round*(.) function. The frequencies of the high-frequency and low-frequency fringes are represented by f_h and f_l, respectively.

According to Eq. (11), the reliability of phase unwrapping is related to the fringe order $k(x, y)$. The

numerator in the second equation of Eq. (11) determines the magnitude of the error in the fringe order $k(x, y)$. Assuming the numerator is represented by ΔM_1, its value should satisfy the following condition; otherwise, phase unwrapping errors may occur.

$$\Delta M = \left|(f_h / f_l)\psi_l(x, y) - \varphi_h(x, y)\right| < \pi. \tag{12}$$

The variance of phase error of dual-frequency heterodyne phase expansion method ΔM_1 is as follows:

$$\begin{aligned} \sigma_{\Delta M_1}^2 &= \left(\frac{f_h}{f_1}\right)^2 \times \sigma_{\psi_1}^2 + \sigma_{\varphi_h}^2 - 2\frac{f_h}{f_1} Cov\left(\psi_1, \varphi_h\right) \\ \Rightarrow \sigma_{\Delta M_1}^2 &= \left(\frac{f_h}{f_1}\right)^2 \times \sigma_{\psi_1}^2 + \sigma_{\varphi_h}^2 \approx \left(\frac{f_h}{f_1}\right)^2 \frac{\sigma^2}{b^2} \end{aligned} . \tag{13}$$

For the dual-frequency four-step phase-shifting method, if the camera captures two sets of fringes with high-frequency f_h =31 and low-frequency f_l = 30, the variance of ΔM_1 can be deduced according to Eq. (13).

$$\begin{aligned} \sigma_{\Delta M_1}^2 &= \left(\frac{f_h}{f_1}\right)^2 \times \frac{\sigma^2}{b^2} + \frac{2\sigma^2}{4b^2} \\ &\approx \left(\frac{f_h}{f_1}\right)^2 \times \frac{\sigma^2}{b^2} \\ &\approx 961 \times \frac{\sigma^2}{b^2} \end{aligned} . \tag{14}$$

For the proposed method, we first consider the selection of fringe frequencies. The choice of ΔM value directly affects the quality of phase unwrapping. In the variance of ΔM, the ratio of high and low fringe frequencies affects the magnitude of the variance. In Eq.(14), the coefficient of the variance is the square of f_h/f_1. It can be seen that if the ratio of f_h to f_1 is larger, the variance will be larger. This method only performs first-order phase unwrapping. If the order is increased, the ratio can be reduced, which can lower the variance. Therefore, the proposed method designs two sets of fringes: one set has a frequency of f=15, and the other set has a frequency of $2f$+1=31. The two sets of fringes are combined using the heterodyne method to obtain the wrapped phase with a frequency of 16. Then, the wrapped phase with a frequency of 1 is obtained by subtracting the wrapped phase of the first set of fringes. The phase unwrapping process is divided into two stages, which can reduce the coefficient of variance, i.e. the frequency ratio (31/16, 16/1), and improve the reliability of phase unwrapping.

$$\begin{cases} \Delta M_2 = (f_{h_3} / f_{h_4})\psi_{h_4}(x, y) - \varphi_{h_3}(x, y) \\ \Delta M_3 = (f_{h_1} / f_{h_3})\psi_{h_3}(x, y) - \varphi_{h_1}(x, y) \end{cases}. \tag{15}$$

The variance of the error in Eq. (15) is

$$\begin{cases} \sigma_{\Delta M_2}^2 = \left(\frac{f_{h_3}}{f_{h_4}}\right)^2 \times \sigma_{\psi_{h_4}}^2 + \sigma_{\varphi_{h_3}}^2 - 2\frac{f_{h_3}}{f_{h_4}} Var\left(\psi_{h_4}, \varphi_{h_3}\right) \\ \Rightarrow \sigma_{\Delta M_2}^2 = \left(\frac{f_{h_3}}{f_{h_4}}\right)^2 \times \sigma_{\psi_{h_4}}^2 + \sigma_{\varphi_{h_3}}^2 \approx \left(\frac{f_{h_3}}{f_{h_4}}\right)^2 \times \frac{3\sigma^2}{2b^2} \\ \sigma_{\Delta M_3}^2 = \left(\frac{f_{h_1}}{f_{h_3}}\right)^2 \times \sigma_{\psi_{h_3}}^2 + \sigma_{\varphi_{h_1}}^2 - 2\frac{f_{h_1}}{f_{h_3}} Var\left(\psi_{h_3}, \varphi_{h_1}\right) \\ \Rightarrow \sigma_{\Delta M_3}^2 = \left(\frac{f_{h_1}}{f_{h_3}}\right)^2 \times \sigma_{\psi_{h_3}}^2 + \sigma_{\varphi_{h_1}}^2 \approx \left(\frac{f_{h_1}}{f_{h_3}}\right)^2 \times \frac{\sigma^2}{b^2} \end{cases}. \tag{16}$$

According to Eq. (16), we can obtain:

$$\begin{cases} \sigma_{\Delta M_2}^2 \approx \left(\dfrac{16}{1}\right)^2 \dfrac{3\sigma^2}{2b^2} \approx 384 \times \dfrac{\sigma^2}{b^2} \\ \sigma_{\Delta M_3}^2 \approx \left(\dfrac{31}{16}\right)^2 \dfrac{\sigma^2}{b^2} \approx 3.75 \times \dfrac{\sigma^2}{b^2} \end{cases}. \tag{17}$$

By comparing Eq. (14) with Eq. (17), we can see that the variance of ΔM_2 in the first phase unwrapping stage of the proposed method is reduced by 60.04% compared to the variance of ΔM_1 obtained by the $4f_h+4f_l$ method. Moreover, the variance of ΔM_3 in the second phase unwrapping stage of the proposed method is reduced by 99.02% compared to the first stage, which makes the error almost negligible compared to the first phase unwrapping stage. Therefore, the advantages of the proposed method over the $4f_h+4f_l$ method lie in its ability to significantly reduce the error of 3D reconstruction without changing the number of fringes, enhance the noise immunity of the dual-frequency phase-shifting method, and improve the accuracy of 3D measurements.

3. Experiments

To validate the effectiveness and feasibility of the proposed method in this paper, we conducted experimental verification of the method and performed several comparative experiments. The experimental setup included a portable computer (CPU: Intel Core i5-5600H), a projector manufactured by Texas Instruments (DLP LightCraft 4500), and a Daheng Imaging camera (MER-131-210U3M). The experiments for the proposed method and the comparative methods were conducted in the same environment, using various test objects. The projected fringe frequencies for the proposed algorithm were f_4=31 and f_3=15. For the comparative experiments, the projected fringe frequencies were high-frequency f_h=31 and low-frequency f_l=30.

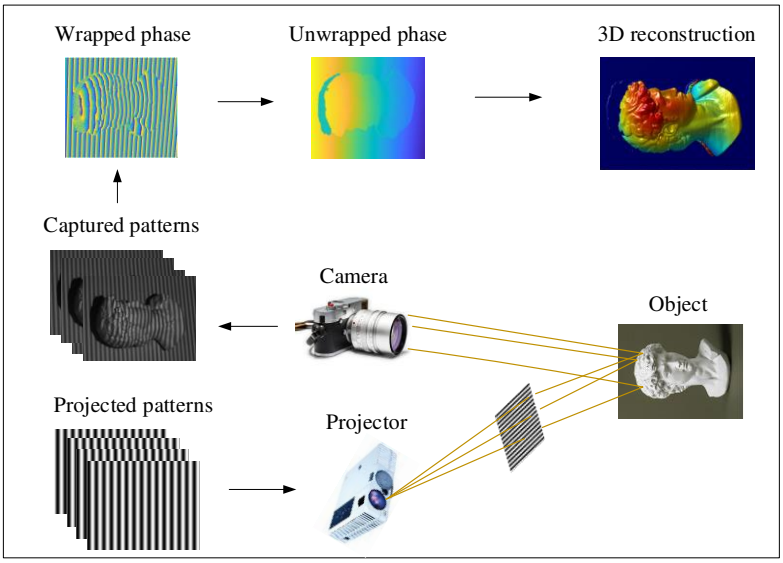

Fig. 3. The principle diagram of FPP.

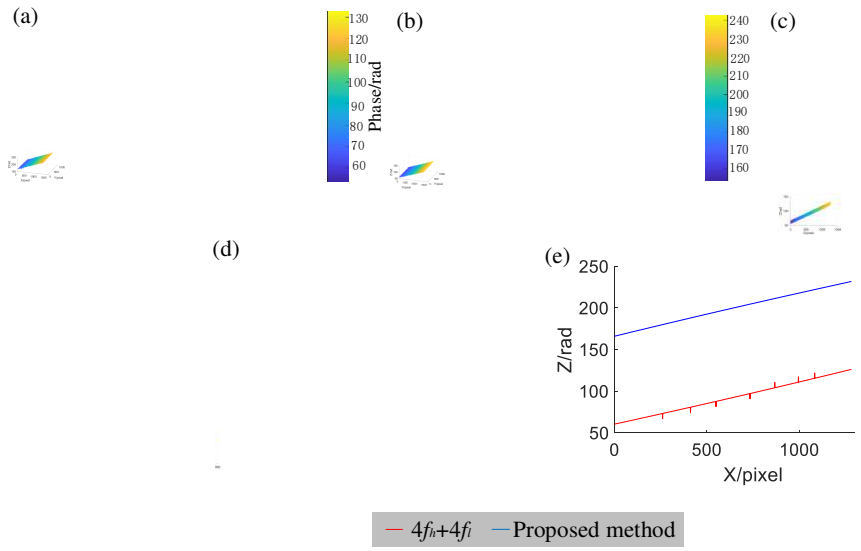

Fig. 4. Comparison of phase errors caused by noise in the unfolded phase of reference fringes between the $4f_h+4f_l$ method and the proposed method. (a) Top view of the unwrapped phase of reference fringes for the $4f_h+4f_l$ method. (b) Top view of the unwrapped phase of reference fringes for the proposed method. (c) Front view of the unwrapped phase of reference fringes for the $4f_h+4f_l$ method. (d) Front view of the unwrapped phase of reference fringes for the proposed method. (e) The unwrapped phase of reference fringes for both methods at the 380th row.

In sections 2.2 and 2.3, we have analyzed the phase errors of both methods in detail. For the $4f_h+4f_l$ method (with fringe frequencies f_h=31 and f_l=30), there is only one phase unwrapping stage during the phase unwrapping process. However, due to the larger frequency ratio (f_h/f_l=31), this results in larger phase errors caused by noise. The variance of the phase errors caused by noise increases with the square of the frequency ratio. On the other hand, for the proposed method (with fringe frequencies f_4=31 and f_3=15), there are two phase unwrapping stages. In the first stage, the phase is unwrapped at a frequency of 16, and in the second stage, the phase is unwrapped at a frequency of 31. In the first stage, the frequency ratio (f_2/f_1=16) is relatively small, leading to smaller phase errors during this stage. Compared to the $4f_h+4f_l$ method, the coefficient of variance of the phase errors caused by noise in the first stage is reduced by approximately 60.04%. In the second stage, the frequency ratio (f_4/f_2≈1.93) is significantly reduced compared to the first stage (reduced by approximately 87.94%). This reduction in frequency ratio leads to a decrease of approximately 99.02% in the coefficient of variance of the phase errors caused by noise. As a result, the phase errors caused by noise in the second stage of the unwrapped phase are further reduced. Overall, the proposed method achieves smaller phase errors caused by noise in the unwrapped phase compared to the $4f_h+4f_l$ method.

Table 1. Comparison of coefficients of variance for two methods

Variance coefficient	The first stage	The second stage
$4f_h+4f_l$ method	961	
Proposed method	384	3.75

In Fig. 4, we can observe that in Fig. 4(c), the phase errors in the planar unwrapped phase using the $4f_h+4f_l$ method are more densely distributed and there are a larger number of errors. In contrast, in Fig. 4(d), the phase errors in the planar unwrapped phase using the proposed method are sparser, with a noticeable reduction in the number of errors. By comparing the planar unwrapped phases of both methods in row 380 in Fig. 4(e), it can be seen that the unwrapped phase using the proposed method is smoother

and has no errors in that row. However, in the case of the $4f_h+4f_l$ method, multiple phase errors are present in that row.

The second measurement object consists of two metallic objects, which are commonly used in people's daily lives and have high measurement values. Figs. 5(a) and (f) show the results of 3D reconstruction of the metallic objects using the $4f_h+4f_l$ method and the proposed method, respectively. Figs. 5(b)-(f) present the 3D rotated views of the measurement results from different perspectives, facilitating visual comparison.

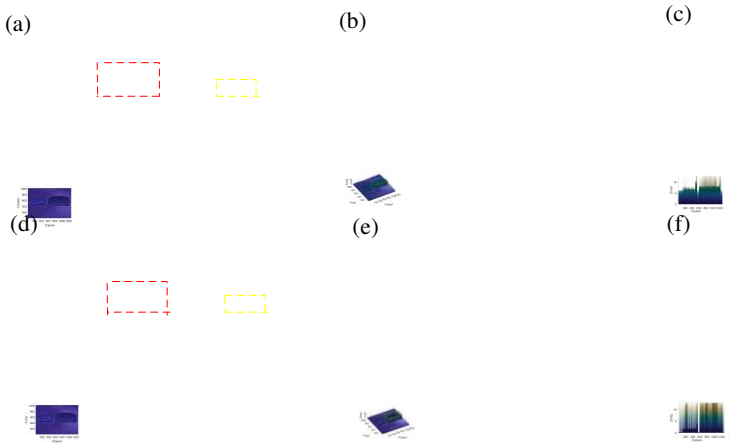

Fig. 5. Compares the 3D reconstruction results of the metallic object using the $4f_h+4f_l$ method and the proposed method. (a) Shows the 3D reconstruction results using the $4f_h+4f_l$ method. (b) The first perspective after rotation of the 3D reconstruction results using the $4f_h+4f_l$ method. (c) The second perspective after rotation of the 3D reconstruction results using the $4f_h+4f_l$ method. (d) The 3D reconstruction results using the proposed method. (e) The first perspective after rotation of the 3D reconstruction results using the proposed method. (f) The second perspective after rotation of the 3D reconstruction results using the proposed method.

By comparing Figs. 5(b) and (d), we can observe that there are more errors in Fig. 5(b) than in Fig. 5(d). Moreover, on the reconstructed surface of the object, the number of errors generated by the 3D reconstruction results using the proposed method is significantly lower compared to those generated by the $4f_h+4f_l$ method. In Figs. 5(c) and (e), it can be seen that the 3D reconstruction results using the $4f_h+4f_l$ method exhibit a higher density of errors, while the errors in the 3D reconstruction results using the proposed method are significantly reduced and sparsely distributed. Thus, the quality of the 3D reconstruction using the proposed method is superior to that using the $4f_h+4f_l$ method.

Based on the localized zoomed-in comparison of the 600th-row phase in Fig. 8, we can observe that the red line (Proposed method) exhibits smoother variation with smaller fluctuations in both upward and downward changes. On the other hand, the blue line ($4f_h+4f_l$ method) shows more oscillations and larger amplitude in comparison to the red line (Proposed method). Hence, it can be concluded that the 3D reconstruction results obtained using the proposed method are superior to those obtained using the $4f_h+4f_l$ method.

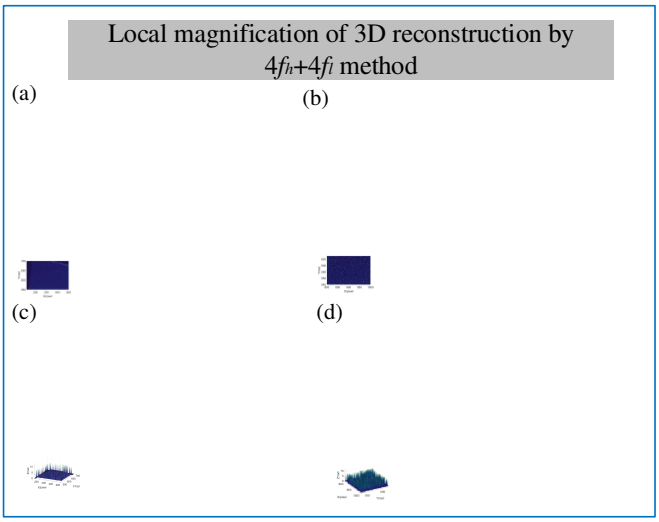

Fig. 6. Local magnification of 3D reconstruction by $4f_h$+$4f_l$ method. (a) A magnified view of the red dashed region in Fig. 5(a). (b) A magnified view of the yellow dashed region in Fig. 5(a). (c) The rotational perspective of Fig. 6(a). (d) The rotational perspective of Fig. 6(b).

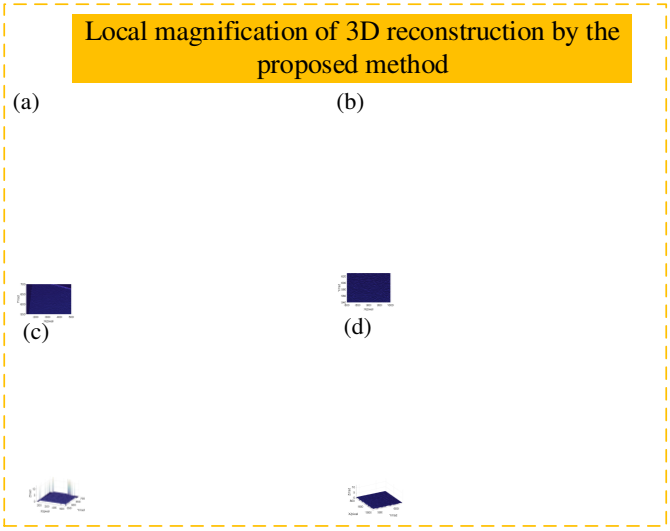

Fig. 7. Local magnification of 3D reconstruction by proposed method. (a) A magnified view of the red dashed region in Fig.5(f). (b) a magnified view of the yellow dashed region in Fig.5(f). (c) the rotational perspective of Fig. 7(a). (d) the rotational perspective of Fig. 7(b).

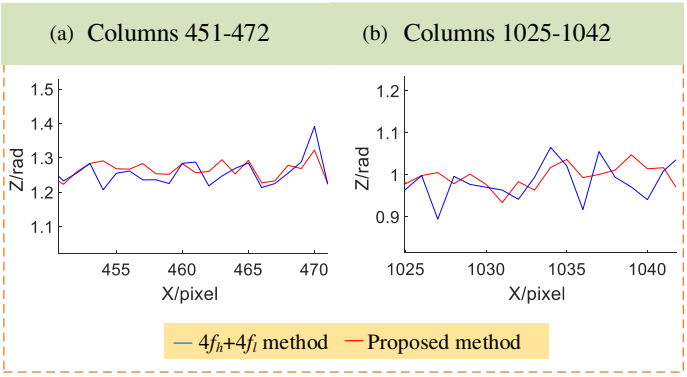

Fig. 8. Comparison of phase local amplification of a line extracted from the results of 3D reconstruction of metal workpieces based on different methods. (a) The picture of columns 451 to 472 phase magnification contrast. (b) The picture of columns 1025 to 1042 phase magnification contrast.

To enhance the reliability of the proposed method, a more complex surface was chosen as the third test object, namely the backside of a David plaster model. The surface of the David plaster model has intricate details, which can further validate the advantages of the proposed method. Fig. 9 shows the 3D reconstruction results of the backside of the David plaster model using both the $4f_h$+$4f_l$ method and the proposed method.

By comparing Figs. 9(b) with (f), and Fig. 9(c) with (g), we can observe that there are significantly more errors in Figs. 9(b) and (c) compared to Figs. 9(f) and (g). In Fig. 9(b), the majority of errors are distributed along the plane and the edges of the David plaster model, while the phase errors on the surface of the David plaster model are relatively minimal. In contrast, in Fig. 9(f), the errors are more concentrated around the edges of the David plaster model, and there are almost no phase errors on the surface. Furthermore, comparing Fig. 9(d) with Fig. 9(h), we can see that the surface of the object in Fig. 9(d) is irregular and rough, with several concave regions, while in Fig. 9(h), the surface is smooth and even, with significantly fewer concave regions. To further validate the reliability of the method, we extracted a row of phases for comparison.

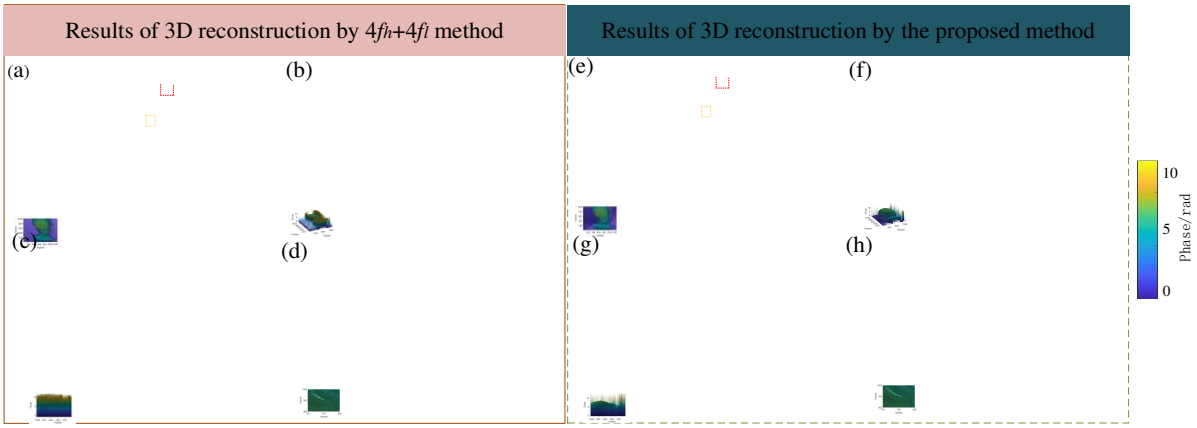

Fig. 9. The results of 3D reconstruction of the back of the plaster of David are based on two different methods. (a) 3D reconstruction results by $4f_h$+$4f_l$ method. (b) First view of the 3D reconstruction results obtained using the $4f_h$+$4f_l$ method after rotation. (c) Second view of the 3D reconstruction results obtained using the $4f_h$+$4f_l$ method after rotation. (d) Local magnification of the red dashed area in Fig. 9(a). (e) The 3D reconstruction results of the proposed method. (f) First view of the 3D reconstruction results obtained using the proposed method after rotation. (g) Second view of the 3D reconstruction results obtained using the proposed method after rotation. (h) Local magnification of the red dashed area in Fig. 9(e).

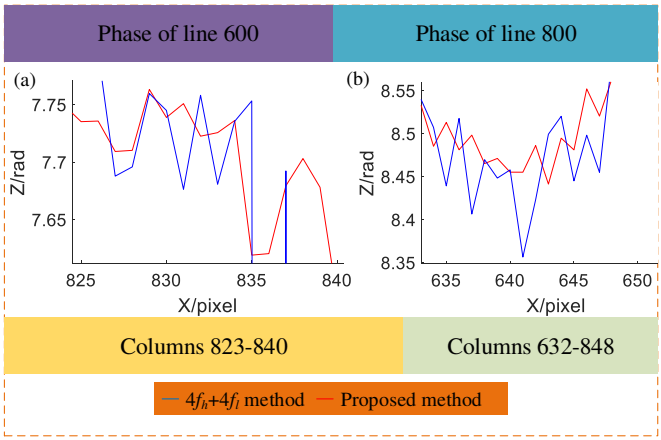

Fig. 10. Comparison of phase local amplification of a line extracted from the 3D reconstruction results of two different methods on the back of gypsum David. (a)The picture of columns 823 to 843 phase magnification contrast. (b) The picture of columns 632 to 848 phase magnification contrast.

Fig. 10(a) shows the enlarged view of the extracted phase on the 600th row after 3D reconstruction of the backside of the David plaster model. Fig. 10(b) displays the enlarged view of the extracted phase on the 800th row. From Fig. 10, it can be observed that the blue line ($4f_h$+$4f_l$ method) exhibits larger variations in amplitude, while the red line (proposed method) shows a smoother and more gradual change. In Fig. 10(a), the $4f_h$+$4f_l$ method reveals two instances of phase errors, whereas the proposed method exhibits no phase errors. This indicates that the $4f_h$+$4f_l$ method results in more surface wrinkles, larger variations in amplitude, and potential phase errors, while the proposed method yields a smoother surface, gradual changes, and fewer errors.

While the proposed method significantly reduces phase errors in the 3D reconstruction of object surfaces, there are instances where small holes may appear. Comparing the yellow box region in Figs. 9(a) and (e), we can observe that Fig. 9(e) contains small holes, indicated by phase values of zero. To address this issue, we propose using an inpainting method to fill the holes in Fig. 9(e), The data lost by the hole is repaired by averaging the phase around the hole.

In Fig. 11, we can observe the presence of small holes in the red boxed area of the 3D reconstruction results obtained using the proposed method. After zooming in on the yellow boxed region, the holes become more apparent. Comparing Figs. 11(g) and (h), we can see that Fig. 11(g) has no holes, but it exhibits more phase errors in the surrounding area. On the other hand, Fig. 11(h) does have holes, but the surrounding phase errors are relatively less. When compared to both of them, Fig. 11(i) demonstrates that the repaired holes have significantly reduced in size and there are fewer phase errors in the surrounding area. This confirms the effectiveness of the proposed method and indicates that the 3D reconstruction results obtained using the proposed method are superior to those obtained using the $4f_h$+$4f_l$ method.

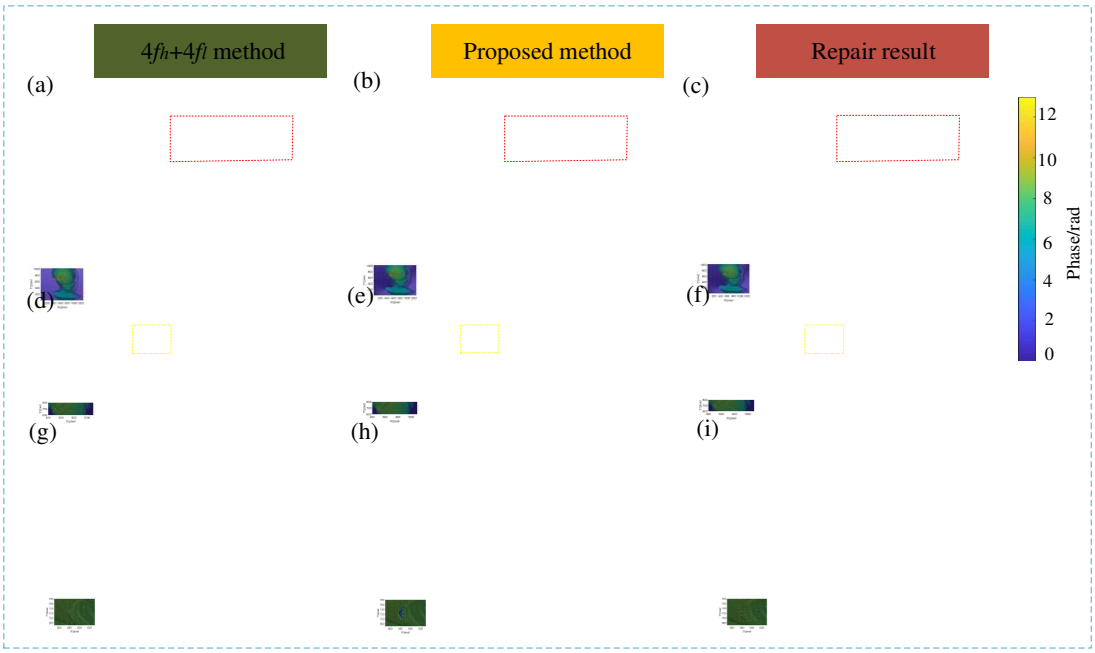

Fig. 11. Comparison of repair results. (a) 3D reconstruction results by $4f_h$+$4f_l$ method. (b) 3D reconstruction results of the proposed method. (c) The result of 3D reconstruction after hole repair. (d) The enlarged view of the red boxed area in Fig. 11(a). (e) The enlarged view of the red boxed area in Fig.

11(b). (f) The enlarged view of the red boxed area in Fig. 11(c). (g) The enlarged view of the yellow boxed area in Fig. 11(d). (h) The enlarged view of the yellow boxed area in Fig. 11(e). (i) The enlarged view of the yellow boxed area in Fig. 11(f).

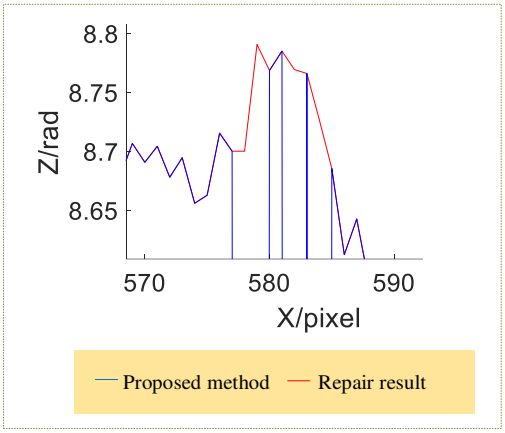

Fig. 12. Comparison of phase amplification of extracted row before and after repair.

In Fig. 12, it can be observed that the blue vertical line region exhibits missing phase data, while the red line represents the filled-in phase data, effectively repairing the holes.

Table 2. Comparison of phase error counts.

The number of phase errors	Metal object experiment	David's plaster backside experiment
$4f_h+4f_l$ method	21162	12527
Proposed method	5099	1079

From Table 2, it can be observed that in both experiments, the number of errors in 3D reconstruction using the proposed method is less than that of the $4f_h+4f_l$ method. Specifically, in the metal object experiment, the proposed method reduces the error count by 75.90%, while in the David gypsum backside experiment, the proposed method reduces the error count by 91.39%.

4. Conclusion

The phase-shifting method can extract the wrapped phase with high accuracy in FPP. Temporal phase unwrapping, which unfolds the wrapped phase pixel by pixel based on multiple wrapped phases at different frequencies, is capable of handling highly discontinuous and isolated complex surfaces, offering high precision and reliability. However, the dual-frequency phase unwrapping method, which only requires two fringe patterns, suffers from reduced noise resistance, resulting in decreased accuracy in 3D measurement. In this paper, a method is proposed to enhance the noise resistance of the dual-frequency phase unwrapping method. By increasing the number of phase unwrapping iterations and reducing the fringe frequency ratio during the unwrapping stage, the phase errors in 3D reconstruction results are minimized. The correctness of the proposed method is verified through theoretical analysis and experimental comparisons. The experiments demonstrate that the $4f_h+4f_l$ method exhibits wrinkled surfaces and higher phase errors in 3D reconstruction, while the proposed method produces smoother surfaces with reduced phase errors. In the metal object experiment, the proposed method reduces the error count by 75.90% compared to the traditional $4f_h+4f_l$ method, and in the David gypsum backside experiment, the error count is reduced by 91.39%. The effectiveness of the proposed method is validated through theoretical analysis and experiments.

Disclosures. The authors declare no conflicts of interest.

Reference

[1] W. C. Liu, L. G. Zhang, X. L. Zhang, and L. F. Han. 3D Snow Sculpture Reconstruction Based on Structured-Light 3D Vision Measurement. Appl Sci-Basel. 11(8)(2021) 3324.

[2] H. M. Huang, G. H. Liu, K. R. Duan, J. Y. Yuan. 3D reconstruction of structured light based on infrared MEMS. J. Laser Appl. 33(4)(2021) 042035.

[3] Z. W. Cai, X. L. Liu, G. Pedrini, W. Osten, X. Peng. Structured-light-field 3D imaging without phase unwrapping. Opt Laser Eng. 129(2020) 106047.

[4] L. Wang, D. Q. Liu, R. W. Qiu, J. Q. Tao. 3D reconstruction from structured-light profilometry with dual-path hybrid network. Eurasip J Adv Sig PR.14(2022).

[5] J. Zhang, B. Luo, X. Su, L. Li, B. W. Li, S. Zhang, and Y. J. Wang. A convenient 3D reconstruction model based on parallel-axis structured light system. Opt Laser Eng. 138(2021) 106366.

[6] H. Luo, K. Zhang, R. F. Li, Y. Xia, and P. D. Liang.A structured-light 3D sensor-based shape measurement method for casting allowance evaluation.10(2022).

[7] Z. W. LI. Research on structural light 3D measurement technology and system based on digital fringe projection. Huazhong university of science and technology. (2009).

[8] Y. L. Chen, F. Y. Wang, and J. Y. Liu. Non-contact portable three-dimensional palmprint acquisition system based on binocular stereo vision and structured light. Laser Optoelectron P. 59(04)(2022) 0410016.

[9] J. Wu, X. Li , S. Y. Liu, Y. L. Li, and Z. J. Yu. Global three-dimensional reconstruction method for visual detection of aircraft skin damage based on rear positioning. Acta. Opt. Sin. 41(11)(2021) 1115002.

[10] J. J. Yu, J. P. Zhou, R. L. Xue, Y. Xu, and L. Xia. Weld surface quality detection based on structured light and illumination model. Chinese J. Lasers. 49(16)(2022) 1602019.

[11] J. Xu and S. Zhang. Status, challenges, and future perspectives of fringe projection profilometry. Opt. Lasters Eng. 135(2020) 106193.

[12] G. Sansoni and F. Docchio, 3D optical measurements in the field of cultural heritage: the case of the vittoria al-ata of brescia. IEEE T. Instrum. Meas. 54(1)(2005) 359-368.

[13] C. Zuo, S. J. Feng, L. Huang, et al. Phase shifting algorithms for fringe projection profilometry: A review. Opt Laser Eng. 109(2018) 23−59.

[14] T. Y. Tao, Q. Chen, S. J. Feng, et al. High-precision real-time 3D shape measurement using a bi-frequency scheme and multi-view system. Appl Optics. 56(13)(2017) 3646-3653.

[15] C. Jiang, S. Xing, H. W. Guo, Fringe harmonics elimination in multi-frequency phase-shifting fringe projection profilometry. Opt. Express,28(3)(2020) 2838-2856.

[16] C. Zuo, X. L. Zhang, Y. Hu,W. Yin, D. T. Shen, J. X. Zhong, J. Zheng and Q. Chen. Has 3D finally come of age? : an introduction to 3D structured-light sensor. Infrared Laser Eng. 49(3)(2020) 9-53.

[17] I. Din, H. Anwar, I. Syed, H. Zafar, L. Hasan. Projector calibration for pattern projection systems. J Appl Res Technol.12(1)(2015) 80–6 .

[18] S. Zhan, R. Chung R. Use of LCD panel for calibrating structured-light-based range sensing system. IEEE Trans Instrum Meas. 57(11)(2008) 2623–30.

[19] G. Falcao, N. Hurtos, J. Massich. Plane-based calibration of a projector-camera system. VIBOT master. 9(1)(2008) 1–12.

[20] J. Huang, Z. Wang, Q. Xue, Gao J . Calibration of a camera projector measurement system and error impact analysis. Meas Sci Technol. 23(12)(2012)125402.

[21] Zhang X . Projector calibration from the camera image point of view. Opt Eng.48(11)(2009) 117208.

[22] S. J. Feng, C. Zuo, L. Zhang, T. Y. Tao, Y. Hu, W. Yin, J. M. Qian, Q. Chen. Calibration of fringe projection profilometry: A comparative review. Opt. Lasters Eng. 143 (2021) 106622.

[23] C. Rathjen. Statistical properties of phase-shift algorithms, J. Opt. Soc. Am. A. 12(9)(1995) 1997–2008.

[24] C. Zuo, Q. Chen, G. Gu, J. Ren, X. Sui, Y. Zhang, Optimized three-step phase shifting profilometry using the third harmonic injection, Opt. Appl. 43(2)(2013) 393–408.

[25] J. L. Li, L. G. Hassebrook, C. Guan. Optimized two-frequency phase-measuring profilometry light-sensor temporal-noise sensitivity. J Opt Soc Am A.20(1)(2003) 106–15.

[26] M. Servin, JC. Estrada,JA. Quiroga, et al. Noise in phase shifting interferometry. Opt Express. 17(2009) 8789–94.

[27] M. Zhang, Q. Chen, T. Tao, S. Feng, Y. Hu, H. Li, C. Zuo, Robust and efficient multi-frequency temporal phase unwrapping: optimal fringe frequency and pattern sequence selection, Opt. Express. 25(17)(2017) 20381–20399.

[28] J H Wang,Y X Yang,P Xu and J T Liu. Noise-induced phase error comparison in multi-frequency phase-shifting profilometry based on few fringes. Opt Laser Technol. 159(2023) 109034.

[29] J T Liu,P Xu,J H Wang and J Xie. Research on phase error and phase unwrapping reliability of noise interference. Laser Technology. (2023) 1-14.

[30] C. Zuo, L. Huang, M. Zhang, et al. Temporal phase unwrapping algorithms for fringe projection profilometry: A comparative review. Opt Laser Eng. 85(2016) 84-103.